Tunable anomalous Andreev reflection and triplet pairings in spin-orbit-coupled graphene

Razieh Beiranvand,[1,*] Hossein Hamzehpour,[1,†] and Mohammad Alidoust[2,‡]
[1]*Department of Physics, K.N. Toosi University of Technology, Tehran 15875-4416, Iran*
[2]*Department of Physics, Faculty of Sciences, University of Isfahan, Hezar Jerib Avenue, Isfahan 81746-73441, Iran*
(Received 9 May 2016; revised manuscript received 17 August 2016; published 12 September 2016)

We theoretically study scattering process and superconducting triplet correlations in a graphene junction comprised of ferromagnet-RSO-superconductor in which RSO stands for a region with Rashba spin-orbit interaction. Our results reveal spin-polarized *subgap* transport through the system due to an anomalous equal-spin Andreev reflection in addition to conventional backscatterings. We calculate equal- and opposite-spin pair correlations near the F-RSO interface and demonstrate direct link of the anomalous Andreev reflection and *equal-spin* pairings arisen due to the proximity effect in the presence of RSO interaction. Moreover, we show that the amplitude of anomalous Andreev reflection, and thus the triplet pairings, are experimentally controllable when incorporating the influences of both tunable strain and Fermi level in the nonsuperconducting region. Our findings can be confirmed by a conductance spectroscopy experiment and may provide more insights into the *proximity-induced* RSO coupling in graphene layers reported recently in experiments [A. Avsar *et al.*, Nat. Commun. **5**, 4875 (2014); Z. Wang *et al.*, Phys. Rev. Lett. **114**, 016603 (2015); J. B. S. Mendes *et al.*, Phys. Rev. Lett. **115**, 226601 (2015); S. Dushenko *et al.*, Phys. Rev. Lett. **116**, 166102 (2016)].

DOI: 10.1103/PhysRevB.94.125415

I. INTRODUCTION

Ferromagnetism and *s* wave superconductivity are two phases of matter with incompatible order parameters. The interplay of superconductivity and ferromagnetism in a junction platform results in intriguing and peculiar phenomena [1–3]. For instance, in a standard uniform superconductor-ferromagnet-superconductor (S-F-S) junction, supercurrent can go under multiple reversals when varying temperature, exchange field, and junction thickness [4]. These sign reversals are due to the apparence of triplet opposite-spin pairings (OSPs) and thus the oscillation of Cooper pairs' amplitude in the time-reversal broken region, i.e., F [1,2,5,6]. If magnetization in the F region follows a nonuniform pattern a new type of superconducting correlations arises: triplet equal-spin pairings (ESPs). The equal-spin pair correlations are long range and can extensively propagate in materials with uniform magnetization and strong scattering resources [1–3,6]. This long range nature of spin-polarized superconducting correlations has turned the ESPs to a highly attractive perspective in nanoscale spintronics [3,7–13]. Another source to generate the ESPs is a combination of spin orbit interactions and uniform Zeeman field proximitized to a superconducting electrode [16–19]. One of the main advantages of making use of spin orbit interactions to induce the ESPs is an all electrical control over the ESPs [14–21].

Graphene is a single layer of carbon atoms, arranged in hexagonal lattices, with a linear dispersion at low energies and tunable Fermi level that can be simply manipulated by a gate voltage [22,23]. These exceptional characteristics in addition to a long spin relaxation time of moving charged carriers, compared to their counterparts in a standard conductor, has turned graphene to a promising material for spintronics devices [22,23]. Superconductivity, ferromagnetism, and spin orbit interactions can be induced into graphene layers by means of the proximity effect [24–34]. It was experimentally demonstrated that a graphene monolayer can support strong Rashba spin orbit interaction of the order of ∼17 meV by proximity to a semiconducting tungsten disulphide substrate [30]. Recent developments have achieved large proximity-induced ferromagnetism and spin orbit interactions in CVD grown graphene single layers coupled to an atomically flat yttrium iron garnet [31,33,34]. To demonstrate the existence of proximity-induced RSO interaction in the graphene layer, a dc voltage along the graphene layer is measured by spin to charge current conversion which is interpreted as the inverse Rashba-Edelstein effect [31,33,34]. The Edelstein effect was first discussed in connection with the spin polarization of conduction electrons in the presence of an electric current [35]. Furthermore, graphene has the capability of sustaining strain and deformations without rupture [36,37]. The application of strain to graphene layers can result in important and interesting phenomena [38–47]. For example, the interplay of massive electrons with spin orbit coupling in the presence of strain in a graphene layer yields controllable spatially separated spin-valley filtering [38,39]. Therefore, this property can be employed as a means to control the spin-transport graphene-based spintronics devices [46].

In this paper, we incorporate RSO interaction, superconductivity, ferromagnetism, and two different types of strain in a setup of graphene-based F-RSO-S contact (depicted in Fig. 1) and propose an experimentally feasible device to generate "controllable" odd-frequency superconducting triplet correlations. Our results reveal a finite anomalous equal-spin Andreev reflection due to the RSO interaction. We demonstrate that this anomalous reflection results in nonvanishing superconducting ESPs in the ferromagnetic region near the F-RSO interface. We also vary the Fermi level (that can be experimentally achieved using a gate voltage) and the strength of an applied strain and show that by simply tuning these two physical quantities one can suppress the amplitude of opposite-spin

*razieh.beiranvand@gmail.com
†hamzehpour@kntu.ac.ir
‡phymalidoust@gmail.com

 ©2016 American Physical Society

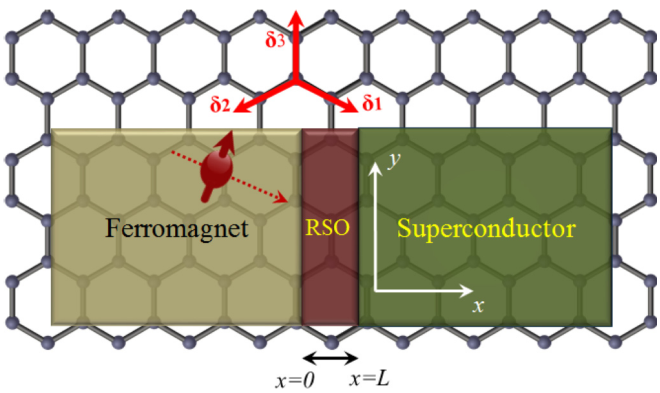

FIG. 1. Schematic of the graphene-based F-RSO-S junction. The junction resides in the xy plane and the RSO region has a thickness of L that extends from $x = 0$ to L. The uniform ferromagnetic and superconducting regions are semi-infinite and constitute interfaces with the RSO region at $x = 0$ and $x = L$. We denote the displacement unit vectors of graphene unit cells by $\boldsymbol{\delta}_{1,2,3}$. A possible trajectory of spin-up particles incident at the F-RSO interface within the F region is shown.

superconducting correlations while simultaneously increasing the equal-spin pairings at the F-RSO interface. Furthermore, we study the charge and spin conductances of the junction and show that the anomalous equal-spin Andreev reflection yields a finite tunable spin-polarized subgap conductance which is experimentally measurable. Such a spectroscopy experiment can be an alternative to those of Refs. [30,31,33,34] for demonstrating the existence of proximity-induced RSO in graphene layers and determining its characteristics. We complement our findings by investigating the system's band structure and discussing its aspects.

The paper is organized as follows. We first summarize the theoretical framework used in Sec. II. The results are discussed in Sec. III in three subsections: in subsec. III A we study the band structure of system and discuss various reflection and transmission probabilities, in subsec. III B the explored anomalous Andreev reflection is linked to the ESPs, and we study the spin and charge conductances in subsec. III C. More details of analytics and calculations are discussed in the Appendix. We finally summarize concluding remarks in Sec. IV.

II. FORMALISM AND THEORY

Because of the specific band shape of monolayer graphene in low energies, carriers in such a system can be treated as massless Dirac fermions [22]. Thus, to describe the low-energy excitations of the structure shown in Fig. 1, one can incorporate the Dirac Hamiltonian with the Bogoilubov–de Gennes equation to reach at a Dirac–Bogoliubov–de Gennes (DBdG) equation in the presence of RSO coupling and exchange field as follows [48]:

$$\begin{pmatrix} \mathcal{H}_{\rm D} + \mathcal{H}_i - \mu^i & \Delta \\ \Delta^\star & \mu^i - \mathcal{T}[\mathcal{H}_{\rm D} - \mathcal{H}_i]\mathcal{T}^{-1} \end{pmatrix} \begin{pmatrix} u \\ v \end{pmatrix} = \varepsilon \begin{pmatrix} u \\ v \end{pmatrix}, \tag{1}$$

where ε is the quasiparticles' energy and u and v refer to the electron and hole parts of spinors, respectively. $\mathcal{H}_{\rm D} = s_0 \otimes (\sigma_x v_x^i k_x + \sigma_y v_y^i k_y)$ is a two dimensional massless Dirac Hamiltonian which governs low energy excitations in one valley of graphene and $\mathcal{T}$ is the time reversal operator [23]. k_x and k_y are components of wave vector in the x and y directions, respectively. σ_i and s_i are Pauli matrices, acting on pseudospin and real spin spaces of graphene (σ_0 and s_0 are 2×2 unit matrices) and natural units are used: $\hbar = 1$. The index i labels F, RSO, or S regions as seen in Fig. 1:

$$\mathcal{H}_i(x) = \begin{cases} \mathcal{H}_{\rm F} = (s_z \otimes \sigma_0)h, & x \leqslant 0, \\ \mathcal{H}_{\rm RSO} = \lambda(s_y \otimes \sigma_x - s_x \otimes \sigma_y), & 0 \leqslant x \leqslant L, \\ \mathcal{H}_{\rm S} = -U_0 s_0 \otimes \sigma_0, & x \geqslant L, \end{cases} \tag{2}$$

where L indicates the thickness of RSO region. Here λ is the energy scale of spin orbit coupling and U_0 is the electrostatic potential in the superconducting region. Because of valley degeneracy in a single layer of graphene, one can simply multiply final results by a factor of two. In a graphene layer under strain $v_x^i \neq v_y^i$ which implies anisotropic Fermi velocity in F, RSO, and S regions. The Fermi energy in each region is shown by μ^i. In the Hamiltonian of F segment, Eq. (2), h represents the exchange field which is added to the Dirac Hamiltonian via the Stoner approach. For simplicity in our calculations, we assume that h is oriented along the z direction without loss of generality [49]. This choice turns the exchange field to a good quantum number that allows for explicitly considering spin-up and -down quasiparticles in the F region and helps having insightful analyses of spin-dependent phenomena in the system. The superconducting gap Δ is a matrix in the particle-hole space (nonzero in $L \leqslant x$) and is given by

$$\Delta = \Theta(x - L) \begin{pmatrix} \Delta_0 e^{i\phi} & 0 & 0 & 0 \\ 0 & \Delta_0 e^{i\phi} & 0 & 0 \\ 0 & 0 & \Delta_0 e^{i\phi} & 0 \\ 0 & 0 & 0 & \Delta_0 e^{i\phi} \end{pmatrix}, \tag{3}$$

in which Δ_0 is the superconducting gap at zero temperature, ϕ is the macroscopic phase of superconductor, and Θ denotes a Heaviside step function. This step function assumption made is valid as far as the Fermi wavelength in the S region is much smaller than F and RSO regions, i.e., $\lambda_F^{\rm S} \ll \lambda_F^{\rm F}, \lambda_F^{\rm RSO}$. Otherwise, a self-consistent approach is favorable to accurately determine the spatial profile of the pair potential [49,50]. We also assume that the F-RSO junction can be described by a step change from the ferromagnetic region to RSO. Although we initially do not consider a smooth change at this junction (that can happen in realistic systems due to the proximity effect), each region eventually gains its own neighbor properties near the boundary by matching their wave functions at this location [23]. We note that such modifications, including weak nonmagnetic impurities and moderately rough interfaces, can only alter the amplitude of scattering probabilities and not the conclusions of our work.

To describe a strained graphene layer, we follow Ref. [37]. Expanding the tight-binding model band structure with arbitrary hopping energies around the Dirac point, one finds

$$\epsilon = \pm \left| \sum_{i=1}^{3} t_i e^{-i\mathbf{k}\cdot\boldsymbol{\delta}} \right|, \tag{4}$$

where $\boldsymbol{\delta}$ is the lattice vector as depicted in Fig. 1. The position of one of the Dirac points $\mathbf{K_D}$ is $(\cos^{-1}(-1/2\eta)/\sqrt{3}a_x, 0)$. Here, we assume $t_{1,2} = t_\vdash$, $t_3 = t$, and $\eta = t_\vdash/t$ in our calculations (see Ref. [51]). These assumptions constitute asymmetric velocities to the Dirac fermions in different directions.

To satisfy the mean field approximation in the S region (which is experimentally relevant) namely, the Fermi wave vector in the superconductor should be much larger than its F and RSO counterparts $k_F^{\mathrm{S}} \gg k_F^{\mathrm{F}}, k_F^{\mathrm{RSO}}$ [23], we consider a heavily dopped superconductor, that is achieved by $U_0 \gg \varepsilon, \Delta_0$ [48]. The resulting wave functions are 1×8 spinors (see the Appendix). We match these wave functions at the boundaries, i.e., at $x = 0$ and $x = L$, and calculate various probabilities of the electron-hole scatterings. We normalize energies by the superconducting gap at zero temperature Δ_0 and lengths by the superconducting coherent length $\xi_S = \hbar v_F/\Delta_0$. The gap of superconductor depends on the temperature (T) and we consider $T = 0.01T_c$ throughout our calculations in which T_c is the critical temperature of superconductor. We also set the length of RSO region fixed at $L = 0.2\xi_S$.

III. RESULTS AND DISCUSSIONS

In this section we present the main results of the paper.

A. Band structure and reflection probabilities

The electronic band structure of each region can provide helpful insights into the properties of system, particularly the various backscatterings and superconducting correlations. To obtain dispersion relations and corresponding spinors in each region, we diagonalize the DBdG Hamiltonian Eq. (1). The system band structure at low energies within F, RSO, and S regions can be expressed by

$$\varepsilon = \pm\mu^{\mathrm{F}} \pm \left[\left(v_x^{\mathrm{F}} k_x^{\mathrm{F}}\right)^2 + \left(v_y^{\mathrm{F}} k_y\right)^2\right]^{1/2} \pm h, \tag{5}$$

$$\varepsilon = \pm\mu^{\mathrm{RSO}} + \zeta\left[\left(v_x^{\mathrm{RSO}} k_x^{\mathrm{RSO}}\right)^2 + \left(v_y^{\mathrm{RSO}} k_y\right)^2 + \lambda^2\right]^{1/2} + \eta\lambda, \tag{6}$$

where $\eta,\zeta = \mp\pm 1$ and

$$\varepsilon = \left[|\Delta_0|^2 + \left(\mu^{\mathrm{S}} + U_0 \pm \sqrt{\left(v_x^{\mathrm{S}} k_x^{\mathrm{S}}\right)^2 + \left(v_y^{\mathrm{S}} k_y\right)^2}\right)^2\right]^{1/2}. \tag{7}$$

Figure 2 illustrates the excitation spectrums in the F, RSO, and S regions. The superconductor is assumed highly doped so that the low energy excitation spectrum is a parabola. In our calculations of the reflection and transmission probabilities we consider a scenario where an electron with spin-up hits the F-RSO interface. Due to the tunable Fermi level in a graphene layer, one can consider three regimes: (i) undoped regime with $\mu = 0$, (ii) low doped limit with $\mu \approx \Delta_0$, and (iii) heavily doped limit with $\mu \gg \Delta_0$. In the RSO region, the band structure has two subbands considering η and ζ ($\{\pm,\mp\}$) signs. Due to the subbands, the RSO region serves as a spin mixer in the transport mechanism. Therefore, when an electron with spin-up hits the F-RSO interface, there is a finite probability for a hole reflection with spin-up. The influences of μ and h are shown in the F region. The solid circles show the electrons in the bands and circles stand for the holes. For a subgap electron with spin-up and $\varepsilon < \mu + h$, corresponding backscattering possibilities are labeled by a–e. The backscattering of $a \to b$ is the normal electron reflection, $a \to c$ is the normal spin-flipped, $a \to d$ is the anomalous Andreev reflection where the backscattered hole lies in the conduction band, and $a \to e$ is the conventional Andreev reflection where the backscattered hole passes through the valance band. We also show a case where the energy of incident electron takes a value of $\varepsilon > \mu + h$ by a'-e' labels. In this

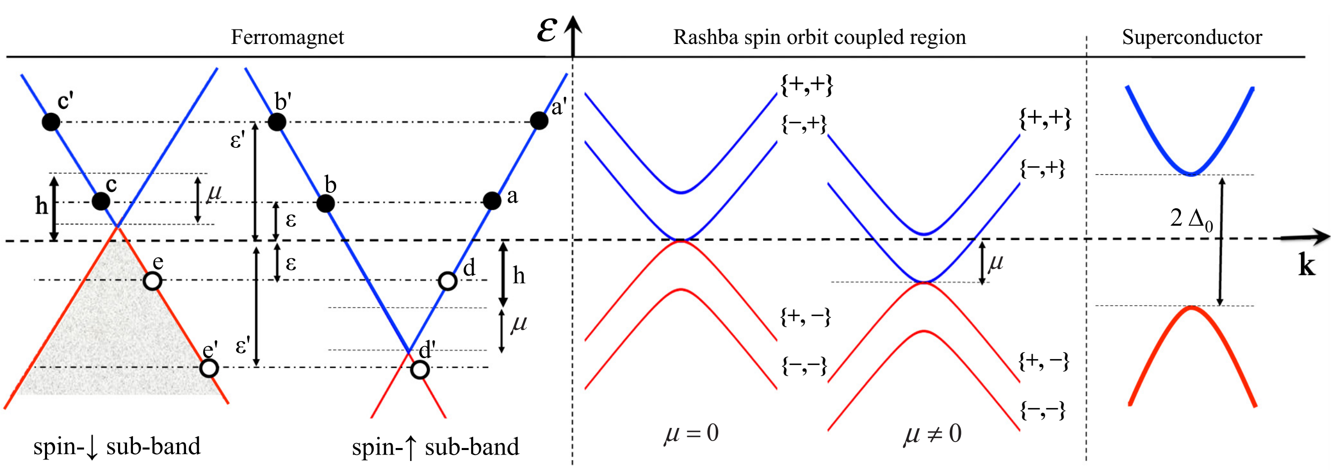

FIG. 2. Band structure of each region. The left panel shows the band structure of F region, illustrating different reflection possibilities including retro and specular reflections discussed in the text. The circles stand for the holes while the solid circles show the electrons. The middle panel is the band structure of RSO region at the charge neutrality point and away from it, i.e., $\mu = 0$ and $\mu \neq 0$, respectively. The $\pm$ signs refer to ζ and η in Eq. (6) due to the band splitting effect of RSO interaction. The right panel is the band structure of a doped superconductor.

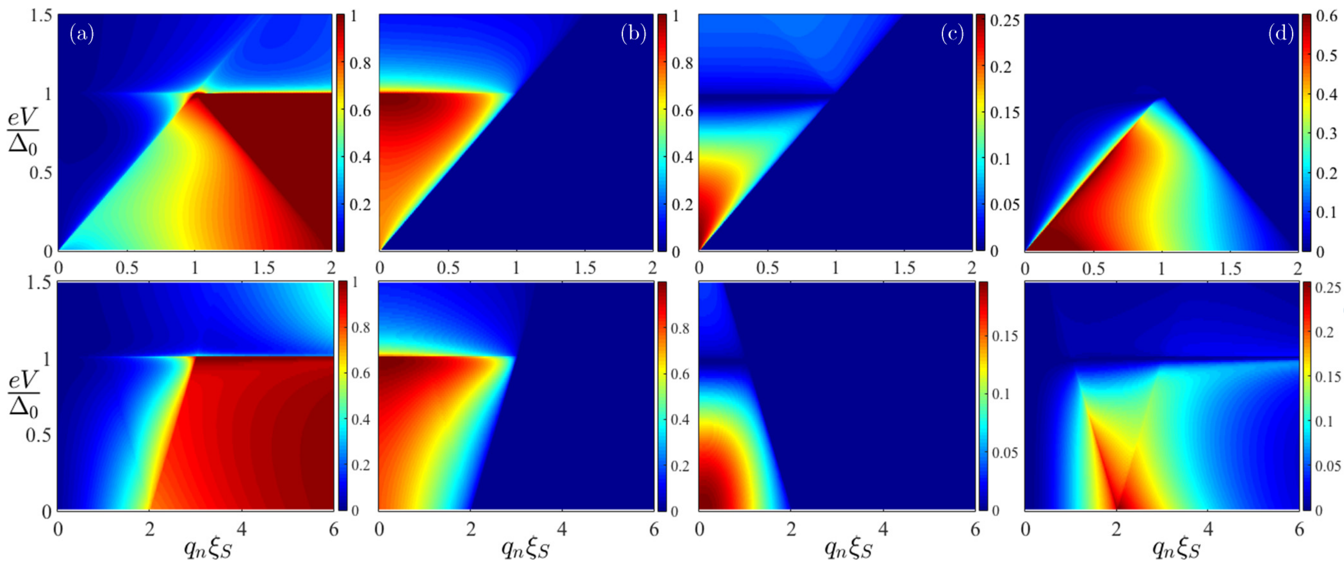

FIG. 3. Backscattering probabilities of an incident spin-up particle at $x = 0$ as a function of applied voltage eV across the junction and the transverse momentum $q_n\xi_S$. (a) Conventional normal reflection $|r_N^{\uparrow}|^2$, (b) conventional Andreev reflection $|r_A^{\downarrow}|^2$, (c) spin-flipped normal reflection $|r_N^{\downarrow}|^2$, and (d) anomalous Andreev reflection $|r_A^{\uparrow}|^2$ vs the transverse component of wave vector q_n. The vertical axis is the applied voltage across the junction. Top row: $\mu = h = \Delta_0$ and $\lambda = 1.5\Delta_0$. Bottom row: $\mu = 0.5\Delta_0$, $h = 7.0\Delta_0$, and $\lambda = 1.5\Delta_0$.

case, the anomalous Andreev reflected hole passes through the valence band.

In an undoped graphene layer, the chemical potential is vanishingly small $\mu \approx 0$. Depending on the energy of the incident particle, a new type of Andreev reflection can take place which is called specular Andreev reflection [48]. The specular Andreev reflection occurs when an electron in the conduction band is converted into a hole in the valence band upon the scattering process. It shows the possibility of an unusual electron-hole conversion in the reflection of relativistic electrons in graphene junctions [48]. In the retro Andreev reflection however electron and hole both lie in the conduction band as shown in Fig. 2. To gain more insights into various reflections that shall be discussed below, we have presented details of calculations and reflections in the Appendix. In the low doped regime ($\mu \approx \Delta_0$), by tuning the system parameters, different effects can occur. (1) $\mu = h \approx \Delta_0$: in this limit, if the RSO parameter is zero ($\lambda = 0$), the Rashba region acts similarly to a normal region with a finite width where the particles can experience resonances upon multiple reflections from boundaries. Hence there are only two reflection probabilities present: (a) conventional normal reflection ($r_N^{\uparrow}$) and (b) either retro Andreev reflection ($\varepsilon \leqslant \mu + h$) or specular Andreev reflection ($\varepsilon \geqslant \mu - h$), depending on the quasiparticle's energy discussed above. The conventional normal reflection dominates at energies below the superconducting gap ($\varepsilon \leqslant \Delta_0$) [48]. In this regime, because μ and exchange field h are equal, the population of spin-down electrons is minority and thus $r_N^{\downarrow} \sim 0$ and $r_A^{\downarrow}$ has a finite probability. (2) At nonzero values of λ, a spin-up particle arriving from the F region can undergo a spin mixing process in the RSO segment. In this limit, in addition to the normal reflection $r_N^{\uparrow}$, the probabilities of anomalous Andreev reflection ($r_A^{\downarrow}$) and unconventional normal reflection ($r_N^{\downarrow}$) have finite amplitudes (see the Appendix). Using this choice of parameters, the conventional Andreev reflected hole is placed in the valence band while the anomalous one passes through the conduction band. Moreover, a hole in the conduction band belongs to the retroreflection process, whereas a hole in the valence band belongs to the specular reflection mechanism [48]. Thus the reflected holes can follow two different processes inside the F region depending on their spin orientation (see left panel of Fig. 2). In a heavily doped graphene $\mu \gg \Delta_0$, the Andreev reflection is of retro type. The propagation of carriers are limited by critical angles that can describe their incident or reflection angles:

$$
\begin{aligned}
\alpha_{e\downarrow}^{c} &= \arcsin\left(\frac{\varepsilon + \mu - h}{\varepsilon + \mu + h}\right),\\
\alpha_{h\downarrow}^{c} &= \arcsin\left(\frac{\varepsilon - \mu + h}{\varepsilon + \mu + h}\right),\\
\alpha_{h\uparrow}^{c} &= \arcsin\left(\frac{\varepsilon - \mu - h}{\varepsilon + \mu + h}\right).
\end{aligned} \tag{8}
$$

As seen, in a regime where $\mu = h \gg \Delta_0$, ε, the critical angles $\alpha_{e,\downarrow}^{c} \approx \alpha_{h,\downarrow}^{c} \approx 0$ vanish. Therefore, their corresponding probabilities do not contribute to the quantum transport. Our investigations demonstrate that in a certain regime of parameter space where $\lambda = \mu = h$, the anomalous Andreev reflection highly dominates in the $eV - q_n$ space. This regime results in zero conventional Andreev reflection while at $\lambda \geqslant h$ the probability of anomalous Andreev reflection at the edge of superconducting gap becomes unity. This effect suggests a spin-polarized Andreev-Klein reflection [52]. Note that the existence of phenomena described above are dependent on the presence of λ.

Figure 3 exhibits backscattering probabilities of an incident particle with spin-up at the F-RSO interface. Throughout our calculations, we consider a fairly narrow region that allows more clear analysis of the ESPs and anomalous Andreev reflection. In the top row panels we set the chemical potential at the superconducting gap $\mu = \Delta_0$ and plot probabilities as a function of an applied voltage across the junction eV/Δ_0 and the transverse particle's momentum $q_n\xi_S$ which is a conserved quantity during the scattering process throughout the system. Here we also consider $v_x^i = v_y^i$ corresponding to zero strain exertion into the system. As seen, in the presence of RSO region, an Andreev reflected hole with the same spin direction as the incident particle $|r_A^\uparrow|^2$ can occur with a finite probability. Furthermore, by calibrating μ, spin-orbit-coupling strength λ, and strain one can suppress the conventional Andreev reflection and simultaneously generate anomalous Andreev reflected holes with a finite probability. We note that $|r_A^\uparrow|^2$ is absent in uniformly magnetized junctions without the RSO region [52–54]. In Fig. 3, bottom row, we change μ to 0.5Δ and $h = 7.0\Delta$. Comparing panels (a)–(d), we see that by tuning the Fermi level one can have a great control over a dominant reflection type at certain applied voltages. For instance, through our specific choice of parameters' value, the anomalous Andreev is well separated from the standard Andreev and spin-flipped normal reflections. Hence, at low voltage differences across the junction, one can access a regime where the anomalous Andreev reflection is the highly dominated reflection simply by tuning the Fermi level. This interesting regime can be determined through a conductance experiment that shall be discussed later. Also, the results can be understood by the band structure analysis presented above and in Eq. (8). Another experimentally controllable parameter that a graphene layer offers is the exertion of an external mechanical tension into the graphene sheet. Our results have found that strain can also change the Andreev and normal reflections the same as what was seen for λ and μ. That is, the strain can render the system to a regime where the anomalous Andreev reflection dominates. We now proceed to discuss the generation of triplet pairs and the properties of charge and spin conductances in a junction of F-RSO-S.

B. Equal- and opposite-spin pairings

It is of fundamental importance to find an experimentally feasible fashion to have control over the amplitude and creation of the equal-spin triplets. Such a control would help to unambiguously reveal the existence of such odd-frequency superconducting correlations in a hybrid structure. As discussed above, the RSO parameter λ is experimentally controlable through a simple external electric field [31,33,34]. The graphene layers have also provided a unique opportunity to tune the Fermi level of a condensed matter system through applying a gate voltage. To further explore the relation between the anomalous Andreev reflections and triplet correlations, we calculate the opposite- and equal-spin pair correlations denoted by f_0 and f_1 [49,55,56]. Following Ref. [49], the OSP and ESP in the graphene system we consider can be expressed by

$$f_0(x,t) = \frac{1}{2}\sum_\beta \xi(t)[u^\uparrow_{\beta,K}v^{\downarrow *}_{\beta,K'} + u^\uparrow_{\beta,K'}v^{\downarrow *}_{\beta,K} - u^\downarrow_{\beta,K}v^{\uparrow *}_{\beta,K'} - u^\downarrow_{\beta,K'}v^{\uparrow *}_{\beta,K}], \tag{9}$$

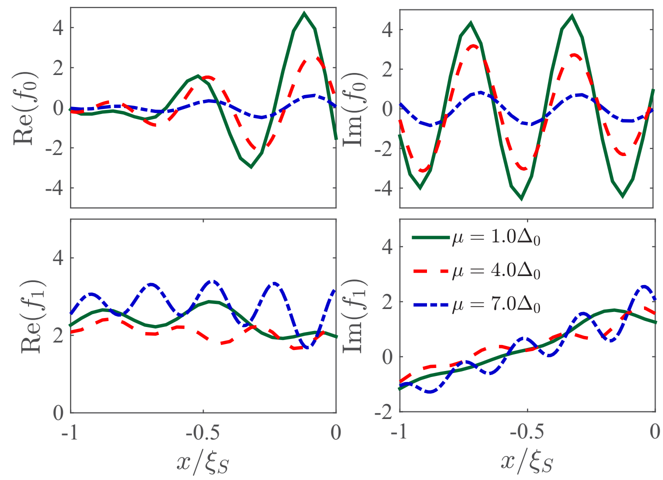

FIG. 4. Real and imaginary parts of OSP (f_0) and ESP (f_1) as a function of position in the F region $x \leqslant 0$. The Fermi energy is set at $\mu = 1.0\Delta_0, 4.0\Delta_0$, and $7.0\Delta_0$ and the voltage difference is assumed constant at $eV = 0.5\Delta_0$. The other parameters are the same as those of Fig. 3, bottom row.

$$f_1(x,t) = -\frac{1}{2}\sum_\beta \xi(t)[u^\uparrow_{\beta,K}v^{\uparrow *}_{\beta,K'} + u^\downarrow_{\beta,K}v^{\downarrow *}_{\beta,K'} + u^\uparrow_{\beta,K'}v^{\uparrow *}_{\beta,K} + u^\downarrow_{\beta,K'}v^{\downarrow *}_{\beta,K}], \tag{10}$$

where K and K' denote different valleys and β stands for A and B sublattices [49]. Here

$$\xi(t) = \cos(\varepsilon t) - i\ \sin(\varepsilon t)\tanh(\varepsilon/2T), \tag{11}$$

in which t is the relative time in the Heisenberg picture [49]. Figure 4 illustrates the real and imaginary parts of OSP (f_0) and ESP (f_1) near the F-RSO interface in the ferromagnetic region shown in Fig. 1, i.e., $x \leqslant 0$. The different curves correspond to different Fermi levels equal to $\mu = 1.0\Delta_0, 4.0\Delta_0, 7.0\Delta_0$. We set the voltage difference across the junction fixed at $eV = 0.5\Delta_0$ whereas other parameters are identical to those of Fig. 3. When we set $\lambda = 0$, the ESP f_1 vanishes and only f_0 remains nonzero. This is consistent with the known findings in a uniform ferromagnet coupled to an s wave superconductor where the only nonvanishing triplet pairing is f_0 [1,2,49,55,56]. A nonzero λ however results in a finite nonvanishing ESP f_1 in addition to the presence of f_0. As seen in Fig. 3, for $\lambda \neq 0$, by calibrating μ one can highly suppress the amplitude of OSP f_0 while increasing f_1. This finding is consistent with those of Ref. [49] for a F-S-F contact with noncollinear magnetization alignments. This is however in stark opposition to a conventional metal counterpart where the tunable chemical potential is absent [49,56–58]. We note that the amplitude of anomalous Andreev reflection discussed in Fig. 3 possesses identical aspects to the ESPs that demonstrates a direct link of the equal-spin parings and the anomalous Andreev reflected holes.

We also introduce two kinds of strain: strain applied along the armchair direction (A strain) and zig-zag direction (Z strain), i.e., y and x directions in Fig. 1, respectively. The applied tension into the graphene lattice causes anisotropic

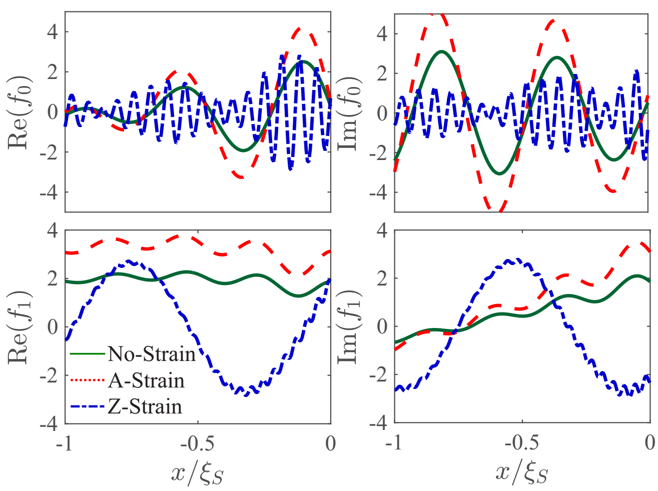

FIG. 5. Real and imaginary parts of OSP (f_0) and ESP (f_1) as a function of position in the F region $x \leqslant 0$ in the presence and absence of A and Z strains at a voltage difference of $eV = 0.5\Delta$ across the contact. The chemical potential is also set at $\mu = 5.0\Delta_0$.

velocities in the x and y directions in each region i: v_x^i, v_y^i and also changes the coupling energy between carbon atoms $t_0 \sim 2.7$ eV. To model the A and Z strain, we consider a strain strength of order of $\sim$20%, which is equivalent to $s = 0.2$ in our model (see Ref. [51]). In this amount of stress s, the coupling energies change to $t_1 = t_2 = 0.96t_0$ and $t_3 = 0.5t_0$ for the A strain, while $t_1 = t_2 = 0.56t_0$ and $t_3 = 1.1t_0$ for the Z strain [51]. Using these parameters, we calculate the corresponding anisotropic velocities of Dirac fermions in strained graphene lattice. Figure 5 exhibits the real and imaginary parts of f_0 and f_1 pair correlations in $x \leqslant 0$ region for a strain-free junction and in the presence of A and Z strain. For simplicity in analysis, we set identical strains in each region, the chemical potential is fixed at $\mu = 5.0\Delta_0$, exchange field $h = 7.0\Delta_0$, $\lambda = 1.5\Delta_0$, and a voltage difference at $eV = 0.5\Delta_0$ across the junction. As seen, the amplitudes of OSPs f_0 and ESPs f_1 are highly influenced by the strain introduced. Interestingly, in the case of Z strain, the amplitude of f_0 rapidly oscillates and diminishes while f_1 becomes less oscillating and smoother. This behavior is suggestive of an experimentally feasible fashion to have control over the amplitude of both f_0 and f_1 so that one can suppress f_0 and simultaneously enhance f_1 in the same system. We have also investigated the backscattering amplitudes in the presence of strain (not shown). As one can expect, in the Z-strain mode, the anomalous Andreev reflection survives while the conventional Andreev reflection is vanishingly small that reaffirms the direct connection of f_1 and the anomalous equal-spin Andreev reflection.

C. Charge and spin conductances

An experimentally measurable quantity in such configuration is the junction conductance. Using the scattering coefficients, one can generalize the theory of Blonder-Tinkham-Klapwijk [59] (see also Ref. [60]) to calculate the

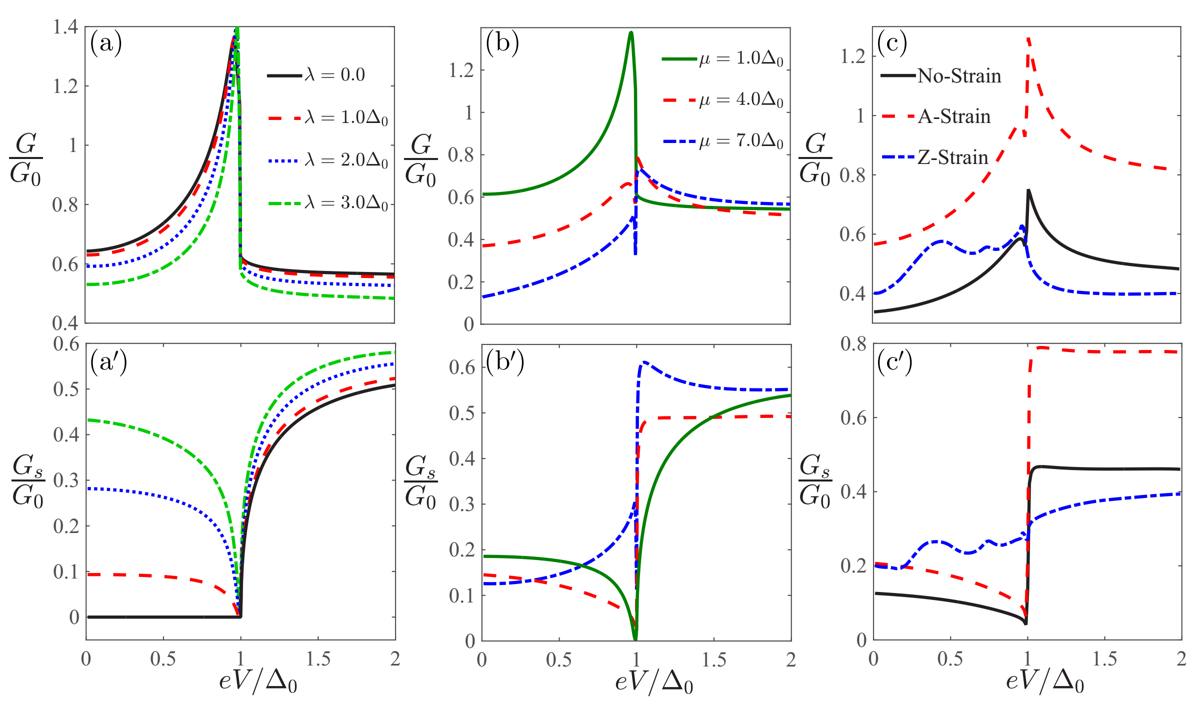

FIG. 6. (a)-(a′) Normalized charge (G) and spin (G_s) conductances as a function of an applied voltage eV across the F-RSO-S junction for different values of the RSO parameter $\lambda = 0.0, 1.0, 2.0,$ and $3.0\Delta_0$. Here $G_0 = G_\uparrow + G_\downarrow$ and we consider $\mu = \Delta_0, L = 0.2\xi_S$, and $h = 7.0\Delta_0$. (b)-(b′) The normalized charge and spin conductances for various values of the chemical potential $\mu = 1.0\Delta_0, 4.0\Delta_0$, and $7.0\Delta_0$ where $\lambda = 1.5\Delta_0$ and $h = 7.0\Delta_0$. (b)-(b′) The normalized charge and spin conductances for A, Z strain, and in the absence of strain at $\mu = 5.0\Delta_0$, $h = 7.0\Delta_0$, and $\lambda = 1.5\Delta_0$.

charge conductance via

$$G = \int dq \sum_{\sigma,\sigma'=\uparrow,\downarrow} G_\sigma \big(1 - |r_N^\sigma|^2 + |r_A^{\sigma'}|^2\big), \tag{12}$$

and the spin-polarized conductance:

$$G_s = \int dq \sum_{\sigma,\sigma'=\uparrow,\downarrow} G_\sigma \big(1 - |r_N^\sigma|^2 + |r_N^{\sigma'}|^2 - |r_A^{\sigma'}|^2 + |r_A^\sigma|^2\big), \tag{13}$$

where $G_\sigma = 2\hbar e|\varepsilon + \mu + \sigma h|$ and the junction width is assumed wide enough so that one can replace $\sum_n \to \int dq$. The behavior of normalized spin and charge conductances are shown in Fig. 6. We have normalized the conductances by $G_0 = G_\uparrow + G_\downarrow$. The presence of exchange energy h in the F region results in an imbalance between particles with different spin directions and causes polarized currents at $eV \geqslant \Delta_0$ (black curve $\lambda = 0$). In the presence of RSO coupling $\lambda \neq 0$, however, due to the possibility of spin mixing in this region, the spin-polarized conductance can be also nonzero in the subgap region $eV \leqslant \Delta_0$. The exchange energy and length of RSO region is kept fixed at $h = 7.0\Delta_0$ and $L = 0.2\xi_S$, respectively. Panels (a) and (a′) illustrate the role of RSO in the charge and spin conductances. As seen, by increasing λ, the spin subgap conductance drastically enhances particularly at zero voltage bias, while the associated charge conductance decreases. The enhancement of spin subgap conductance traces back to the generation of equal-spin triplet correlations (see Fig. 4, corresponding triplet correlations). Figure 6 also shows the effect of chemical potential in panels (b) and (b′). While the chemical potential can reduce the charge subgap conductance, the spin subgap conductance remains about the same at low voltages for the chosen set of parameters. The changes in the spin-polarized conductance is more pronounced at larger voltages. The influence of A and Z strain is shown in (c) and (c′). We see that in the Z-strain mode the spin subgap conductance is almost largest, while the corresponding charge conductance is less than A-strain mode. The conductance behaviors are consistent with the associated backscattering probabilities and superconducting triplet correlations presented in the previous subsections.

IV. CONCLUSION

In conclusion, motivated by recent experiments [30,31,33,34], we have theoretically studied backscattering probabilities, triplet superconducting correlations, and charge/spin conductance in a ferromagnet-Rashba spin-orbit-superconductor graphene-based junction. Our findings offer an experimentally feasible platform for creating tunable superconducting equal-spin triplet correlations. The odd-frequency triplet correlations are formed near the F-RSO interface through an anomalous equal-spin Andreev backscattering. Considering the band structure of system, the anomalous reflection is allowed due to a band splitting in the presence of Rashba spin-orbit coupling in the RSO region. We show that the amplitude of equal-spin pair correlations can be enhanced by varying the Fermi level in nonsuperconducting region, exertion of strain into the graphene layer, and controlling the strength of RSO through an external electric field while the amplitude of opposite-spin pair correlations suppressed simultaneously. The anomalous equal-spin Andreev reflection also causes a nonzero spin-polarized *subgap* conductance. These phenomena can be revealed in a conductance spectroscopy experiment. More importantly, the signatures of the equal-spin pairings on the experimentally observable quantities discussed here can supply suitable insights into the proximity-induced Rashba spin-orbit couplings recently achieved in experiments [30,31,33,34].

ACKNOWLEDGMENTS

We thank M. Salehi for numerous helpful conversations. M.A. also would like to thank K. Halterman for useful discussions. This work was financially supported by the Iran National Science Foundation (INSF).

APPENDIX

The wave functions associated with the dispersion relation in the F region are

$$\begin{aligned}
\psi_{e,\uparrow}^{\mathrm{F},\pm}(x) &= \big(\mathbf{0^2},1,\pm e^{\pm i\alpha_\uparrow^e},\mathbf{0^4}\big)^{\mathbf{T}} e^{\pm ik_{x,\uparrow}^{\mathrm{F},e}x},\\
\psi_{e,\downarrow}^{\mathrm{F},\pm}(x) &= \big(1,\pm e^{\pm i\alpha_\downarrow^e},\mathbf{0^2},\mathbf{0^4}\big)^{\mathbf{T}} e^{\pm ik_{x,\downarrow}^{\mathrm{F},e}x},\\
\psi_{h,\uparrow}^{\mathrm{F},\pm}(x) &= \big(\mathbf{0^4},1,\mp e^{\pm i\alpha_\uparrow^h},\mathbf{0^2}\big)^{\mathbf{T}} e^{\pm ik_{x,\uparrow}^{\mathrm{F},h}x},\\
\psi_{h,\downarrow}^{\mathrm{F},\pm}(x) &= \big(\mathbf{0^4},\mathbf{0^2},1,\mp e^{\pm i\alpha_\downarrow^h}\big)^{\mathbf{T}} e^{\pm ik_{x,\downarrow}^{\mathrm{F},h}x},
\end{aligned} \tag{A1}$$

where $\mathbf{0^n}$ represents a $1 \times n$ matrix with only zero entries and $\mathbf{T}$ is a transpose operator. We assume that the junction width W is enough large so that the y component of the wave vector k_y is a conserved quantity upon the scattering processes and, therefore, we factored out the corresponding multiplication, i.e., $\exp(ik_y y)$. The $\alpha_{e,(h)}^{\uparrow(\downarrow)}$ variables are the propagation angles in the presence of strain and are given by

$$\alpha_{\uparrow,(\downarrow)}^{e(h)} = \arctan\left(\frac{v_y^{\mathrm{F}} q_n}{v_x^{\mathrm{F}} k_{x,\uparrow(\downarrow)}^{\mathrm{F},e(h)}}\right). \tag{A2}$$

The $e(h)$ superscript indicates electron (hole) -like parameters and $\uparrow(\downarrow)$ subscript denotes the spin orientation. The x component of wave vectors are not conserved during the scattering processes and can be expressed by

$$\begin{aligned}
k_{x,\uparrow}^{\mathrm{F},e} &= \big(\hbar v_x^{\mathrm{F}}\big)^{-1}(\varepsilon + \mu^{\mathrm{F}} + h)\cos\alpha_\uparrow^e,\\
k_{x,\downarrow}^{\mathrm{F},e} &= \big(\hbar v_x^{\mathrm{F}}\big)^{-1}(\varepsilon + \mu^{\mathrm{F}} - h)\cos\alpha_\downarrow^e,\\
k_{x,\uparrow}^{\mathrm{F},h} &= \big(\hbar v_x^{\mathrm{F}}\big)^{-1}(\varepsilon - \mu^{\mathrm{F}} - h)\cos\alpha_\uparrow^h,\\
k_{x,\downarrow}^{\mathrm{F},h} &= \big(\hbar v_x^{\mathrm{F}}\big)^{-1}(\varepsilon - \mu^{\mathrm{F}} + h)\cos\alpha_\downarrow^h.
\end{aligned} \tag{A3}$$

We denote $k_y^i \equiv q_n$ that can vary in interval $-\infty \leqslant q_n \leqslant +\infty$. The x component of the wave vector, however, becomes imaginary for larger values of q_n than a critical value q^c. The wave functions for $q_n > q^c$ are decaying functions and, therefore, depending on the junction geometry, are not able to contribute to the transport process. The critical values can be expressed as follows:

$$q^c_{e,\uparrow} = \left(\hbar v^{\mathrm{F}}_y\right)^{-1}|\varepsilon + \mu^{\mathrm{F}} + h|,$$
$$q^c_{e,\downarrow} = \left(\hbar v^{\mathrm{F}}_y\right)^{-1}|\varepsilon + \mu^{\mathrm{F}} - h|,$$
$$q^c_{h,\uparrow} = \left(\hbar v^{\mathrm{F}}_y\right)^{-1}|\varepsilon - \mu^{\mathrm{F}} - h|,$$
$$q^c_{h,\downarrow} = \left(\hbar v^{\mathrm{F}}_y\right)^{-1}|\varepsilon - \mu^{\mathrm{F}} + h|. \tag{A4}$$

In contrast to the intrinsic spin-orbit couplings, the energy spectrum in the presence of RSO is gapless with a splitting of magnitude 2λ between subbands in the RSO region. The wave functions associated with the eigenvalues given in the text can be expressed by

$$\begin{aligned}
\psi^{\mathrm{RSO},\pm}_{e,\eta=+1}(x) &= \left(\mp i f^e_+ e^{\mp i\theta^e_+}, -i, 1, \pm f^e_+ e^{\pm i\theta^e_+}, \mathbf{0^4}\right)^{\mathbf{T}} e^{\pm i k^{\mathrm{RSO},e}_{x,+} x},\\
\psi^{\mathrm{RSO},\pm}_{e,\eta=-1}(x) &= \left(\pm f^e_- e^{\mp i\theta^e_-}, 1, -i, \mp i f^e_- e^{\pm i\theta^e_-}, \mathbf{0^4}\right)^{\mathbf{T}} e^{\pm i k^{\mathrm{RSO},e}_{x,-} x},\\
\psi^{\mathrm{RSO},\pm}_{h,\eta=+1}(x) &= \left(\mathbf{0^4}, \mp i f^h_+ e^{\mp i\theta^h_+}, -i, 1, \pm f^h_+ e^{\pm i\theta^h_+}\right)^{\mathbf{T}} e^{\pm i k^{\mathrm{RSO},h}_{x,+} x},\\
\psi^{\mathrm{RSO},\pm}_{h,\eta=-1}(x) &= \left(\mathbf{0^4}, \pm f^h_- e^{\mp i\theta^h_-}, 1, -i, \mp i f^h_- e^{\pm i\theta^h_-}\right)^{\mathbf{T}} e^{\pm i k^{\mathrm{RSO},h}_{x,-} x}.
\end{aligned} \tag{A5}$$

Here also the transverse component of wave vector is factored out due to the conservation discussion made earlier. The x component of the wave vector, however, is not conserved during the scattering processes:

$$\begin{aligned}
k^{\mathrm{RSO},e}_{x,\eta} &= \left(v^{\mathrm{RSO}}_x\right)^{-1}(\mu^{\mathrm{RSO}} + \varepsilon) f^e_\eta \cos\theta^e_\eta,\\
k^{\mathrm{RSO},h}_{x,\eta} &= \left(v^{\mathrm{RSO}}_x\right)^{-1}(\mu^{\mathrm{RSO}} - \varepsilon) f^e_\eta \cos\theta^h_\eta,
\end{aligned} \tag{A6}$$

and the definition of auxiliary parameters are

$$\begin{aligned}
f^e_\eta &= \sqrt{1 + 2\eta\lambda(\mu^{\mathrm{RSO}} + \varepsilon)^{-1}}, \quad \theta^e_\eta = \arctan\left(\frac{q_n v^{\mathrm{RSO}}_y}{v^{\mathrm{RSO}}_x k^{\mathrm{RSO},e}_{x,\eta}}\right),\\
f^h_\eta &= \sqrt{1 + 2\eta\lambda(\mu^{\mathrm{RSO}} - \varepsilon)^{-1}}, \quad \theta^h_\eta = \arctan\left(\frac{q_n v^{\mathrm{RSO}}_y}{v^{\mathrm{RSO}}_x k^{\mathrm{RSO},h}_{x,\eta}}\right),
\end{aligned} \tag{A7}$$

where $\theta^{e(h)}_\eta$ are the electron and hole propagation angles in the region with spin-orbit interaction. We note that if the transverse component of wave vector goes beyond a critical value q^c, the same as what was discussed for the ferromagnet region, the wave functions turn to evanescent modes. Here, however, since the RSO region is sandwiched between F and S regions, the evanescent modes contribute to the quantum transport process. We thus take both the propagating and decaying modes into account throughout our calculations.

In the superconductor region, U_0 denotes the electrostatic potential that is very large ($U_0 \gg 1$) in actual experiments compared to other system energy scales so that the step function assumption made above for the pair potential can be a good approximation in numerous realistic cases. The wave functions in the superconducting region are given by

$$\begin{aligned}
\psi^{\mathrm{S},\pm}_{e,1}(x) &= (e^{+i\beta}, \pm e^{+i\beta}, \mathbf{0^2}, e^{-i\phi}, \pm e^{-i\phi}, \mathbf{0^2})^{\mathbf{T}} e^{\pm i k^{\mathrm{S},e}_x x},\\
\psi^{\mathrm{S},\pm}_{e,2}(x) &= (\mathbf{0^2}, e^{+i\beta}, \pm e^{+i\beta}, \mathbf{0^2}, e^{-i\phi}, \pm e^{-i\phi})^{\mathbf{T}} e^{\pm i k^{\mathrm{S},e}_x x},\\
\psi^{\mathrm{S},\pm}_{h,1}(x) &= (e^{-i\beta}, \mp e^{-i\beta}, \mathbf{0^2}, e^{-i\phi}, \mp e^{-i\phi}, \mathbf{0^2})^{\mathbf{T}} e^{\pm i k^{\mathrm{S},h}_x x},\\
\psi^{\mathrm{S},\pm}_{h,2}(x) &= (\mathbf{0^2}, e^{-i\beta}, \mp e^{-i\beta}, \mathbf{0^2}, e^{-i\phi}, \mp e^{-i\phi})^{\mathbf{T}} e^{\pm i k^{\mathrm{S},h}_x x}.
\end{aligned} \tag{A8}$$

The parameter β is responsible for the electron-hole conversions at the interface RSO-S and depends on the superconducting gap:

$$\beta = \begin{cases} +\arccos(\varepsilon/\Delta_0), & \varepsilon \leqslant \Delta_0,\\ -i\,\mathrm{arccosh}(\varepsilon/\Delta_0), & \varepsilon \geqslant \Delta_0. \end{cases} \tag{A9}$$

Similar expressions to those found for the longitudinal component of wave vector in the F and RSO region appear for the S. In the F region, we assume that a right moving electron with spin-up direction hits the interface of F-RSO with energy ε. This particle can reflect back as (a) an electron with spin-up direction (conventional normal reflection), (b) as a hole with spin-down direction (conventional Andreev reflection), (c) as an electron with spin-down direction (spin flipped normal reflection), and (d) as a hole with spin-up direction (anomalous Andreev reflection). Thus the total wave function in the F region can be written as

$$\begin{aligned}
\Psi^{\mathrm{F}}(x) = {}& \left(\mathbf{0^2}, 1, e^{+i\alpha^e_\uparrow}, \mathbf{0^4}\right)^{\mathbf{T}} e^{+i k^{\mathrm{F},e}_{x,\uparrow} x} + r^\uparrow_N\left(\mathbf{0^2}, 1, -e^{-i\alpha^e_\uparrow}, \mathbf{0^4}\right)^{\mathbf{T}}\\
&\times e^{-i k^{\mathrm{F},e}_{x,\uparrow} x} + r^\downarrow_N\left(1, -e^{-i\alpha^e_\downarrow}, \mathbf{0^2}, \mathbf{0^4}\right)^{\mathbf{T}} e^{-i k^{\mathrm{F},e}_{x,\downarrow} x}\\
&+ r^\uparrow_A\left(\mathbf{0^4}, 1, e^{-i\alpha^h_\uparrow}, \mathbf{0^2}\right)^{\mathbf{T}} e^{-i k^{\mathrm{F},h}_{x,\uparrow} x} + r^\downarrow_A\left(\mathbf{0^4}, \mathbf{0^2}, 1, e^{-i\alpha^h_\downarrow}\right)^{\mathbf{T}}\\
&\times e^{-i k^{\mathrm{F},h}_{x,\downarrow} x},
\end{aligned} \tag{A10}$$

where $r^\uparrow_N$, $r^\downarrow_N$, $r^\downarrow_A$, and $r^\uparrow_A$ are the amplitudes of conventional, anomalous normal reflections, conventional, and anomalous Andreev reflections, respectively. When an electron hits the F-RSO interface, it can enter into the RSO region through one of its subbands and reflect back as an electron or hole upon collision with the RSO-S interface. Each subband is a mixture of spin-up and -down due to the presence of RSO coupling. Hence, in the RSO region, $0 \leqslant x \leqslant L$, the total wave function is given by

$$\begin{aligned}
\Psi^{\mathrm{RSO}}(x) = {}& a_1\left(-i f^e_+ e^{-i\theta^e_+}, -i, 1, f^e_+ e^{i\theta^e_+}, \mathbf{0^4}\right)^{\mathbf{T}} e^{i k^{\mathrm{RSO},e}_{x,+} x} + a_2\left(i f^e_+ e^{i\theta^e_+}, -i, 1, -f^e_+ e^{-i\theta^e_+}, \mathbf{0^4}\right)^{\mathbf{T}} e^{-i k^{\mathrm{RSO},e}_{x,+} x}\\
&+ a_3\left(f^e_- e^{-i\theta^e_-}, 1, -i, -i f^e_- e^{i\theta^e_-}, \mathbf{0^4}\right)^{\mathbf{T}} e^{i k^{\mathrm{RSO},e}_{x,-} x} + a_4\left(-f^e_- e^{i\theta^e_-}, 1, -i, i f^e_- e^{-i\theta^e_-}, \mathbf{0^4}\right)^{\mathbf{T}} e^{-i k^{\mathrm{RSO},e}_{x,-} x}\\
&+ a_5\left(\mathbf{0^4}, -i f^h_+ e^{-i\theta^h_+}, -i, 1, f^h_+ e^{i\theta^h_+}\right)^{\mathbf{T}} e^{i k^{\mathrm{RSO},h}_{x,+} x} + a_6\left(\mathbf{0^4}, i f^h_+ e^{i\theta^h_+}, -i, 1, -f^h_+ e^{-i\theta^h_+}\right)^{\mathbf{T}} e^{-i k^{\mathrm{RSO},h}_{x,+} x}\\
&+ a_7\left(\mathbf{0^4}, f^h_- e^{-i\theta^h_-}, 1, -i, -i f^h_- e^{i\theta^h_-}\right)^{\mathbf{T}} e^{i k^{\mathrm{RSO},h}_{x,-} x} + a_8\left(\mathbf{0^4}, -f^h_- e^{i\theta^h_-}, 1, -i, i f^h_- e^{-i\theta^h_-}\right)^{\mathbf{T}} e^{-i k^{\mathrm{RSO},h}_{x,-} x}.
\end{aligned} \tag{A11}$$

As seen, the total wave function in this region involves eight unknown coefficients $a_{1,\dots,8}$ for spin-up and -down particles and holes. Finally, the total wave function in the S region can be written as follows:

$$\Psi^{\mathrm{S}}(x) = t_1(e^{i\beta},e^{i\beta},\mathbf{0}^2,e^{-i\phi},e^{-i\phi},\mathbf{0}^2)e^{ik_x^{\mathrm{S}}x} + t_2(\mathbf{0}^2,e^{i\beta},e^{i\beta},\mathbf{0}^2,e^{-i\phi},e^{-i\phi})e^{ik_x^{\mathrm{S}}x} + t_3(e^{-i\beta},-e^{-i\beta},\mathbf{0}^2,e^{-i\phi},-e^{-i\phi},\mathbf{0}^2)e^{-ik_x^{\mathrm{S}}x} + t_4(\mathbf{0}^2,e^{-i\beta},-e^{-i\beta},\mathbf{0}^2,e^{-i\phi},-e^{-i\phi})e^{-ik_x^{\mathrm{S}}x}. \quad \text{(A12)}$$

Here, the transmission coefficients are denoted by $t_{1,2,3,4}$. The macroscopic phase of superconductivity ϕ plays no role in the geometry considered and thus we set it zero. In the above wave function, we assumed that the S region is in a heavily doped regime, i.e., $U_0 \gg \varepsilon,\Delta_0$. By matching the wave functions at the interfaces, i.e., $\Psi^{\mathrm{F}}(x) = \Psi^{\mathrm{RSO}}(x)$ at $x = 0$ and $\Psi^{\mathrm{RSO}}(x) = \Psi^{\mathrm{S}}(x)$ at $x = L$, we obtain the unknown scattering coefficients. The resulting coefficients however are very large and complicated expressions and we skip presenting them.

[1] A. I. Buzdin, Proximity effects in superconductor-ferromagnet heterostructures, Rev. Mod. Phys. **77**, 935 (2005).

[2] F. S. Bergeret, A. F. Volkov, and K. B. Efetov, Odd triplet superconductivity and related phenomena in superconductor-ferromagnet structures, Rev. Mod. Phys. **77**, 1321 (2005).

[3] M. Eschrig, Spin-polarized supercurrents for spintronics: A review of current progress, Rep. Prog. Phys. **78**, 104501 (2015); Theory of Andreev bound states in SFS junctions and SF proximity devices, arXiv:1509.07818.

[4] V. V. Ryazanov, V. A. Oboznov, A. Y. Rusanov, A. V. Veretennikov, A. A. Golubov, and J. Aarts, Coupling of Two Superconductors Through a Ferromagnet: Evidence for a Junction, Phys. Rev. Lett. **86**, 2427 (2001).

[5] Ya. V. Fominov, A. A. Golubov, and M. Yu. Kupriyanov, Triplet proximity effect in FSF trilayers, JETP Lett. **77**, 510 (2003); S. V. Bakurskiy, N. V. Klenov, I. I. Soloviev, M. Yu. Kupriyanov, and A. A. Golubov, Superconducting phase domains for memory applications, Appl. Phys. Lett. **108**, 042602 (2016).

[6] M. Alidoust and K. Halterman, Proximity induced vortices and long-range triplet supercurrents in ferromagnetic Josephson junctions and spin valves, J. Appl. Phys. **117**, 123906 (2015).

[7] Y. N. Khaydukov, G. A. Ovsyannikov, A. E. Sheyerman, K. Y. Constantinian, L. Mustafa, T. Keller, M. A. UribeLaverde, Yu. V. Kislinskii, A. V. Shadrin, A. Kalabukhov, B. Keimer, and D. Winkler, Evidence for spin-triplet superconducting correlations in metal-oxide heterostructures with noncollinear magnetization, Phys. Rev. B **90**, 035130 (2014).

[8] Y. Kalcheim, O. Millo, A. Di Bernardo, A. Pal, and J. W. A. Robinson, Inverse proximity effect at superconductorferromagnet interfaces: Evidence for induced triplet pairing in the superconductor, Phys. Rev. B **92**, 060501(R) (2015).

[9] K. Halterman and M. Alidoust, Half-metallic superconducting triplet spin valve, Phys. Rev. B **94**, 064503 (2016).

[10] M. G. Flokstra, N. Satchell, J. Kim, G. Burnell, P. J. Curran, S. J. Bending, J. F. K. Cooper, C. J. Kinane, S. Langridge, A. Isidori, N. Pugach, M. Eschrig, H. Luetkens, A. Suter, T. Prokscha, and S. L. Lee, Remotely induced magnetism in a normal metal using a superconducting spin-valve, Nat. Phys. **12**, 57 (2016).

[11] I. V. Bobkova and A. M. Bobkov, Long-range Proximity Effect for Opposite-Spin Pairs in Superconductorferromagnet Heterostructures Under Nonequilibrium Quasiparticle Distribution, Phys. Rev. Lett. **108**, 197002 (2012).

[12] P. D. Sacramento, L. C. Fernandes Silva, G. S. Nunes, M. A. N. Araujo, and V. R. Vieira, Supercurrent-induced domain wall motion, Phys. Rev. B **83**, 054403 (2011).

[13] A. Moor, A. F. Volkov, and K. B. Efetov, Nematic versus ferromagnetic spin filtering of triplet Cooper pairs in superconducting spintronics, Phys. Rev. B **92**, 180506(R) (2015).

[14] I. V. Bobkova and Yu. S. Barash, Effects of spin-orbit interaction on superconductor-ferromagnet heterostructures: Spontaneous electric and spin surface currents, JETP Lett. **80**, 494 (2004).

[15] F. Konschelle, I. V. Tokatly, and F. S. Bergeret, Theory of the spin galvanic effect and the anomalous phase shift φ_0 in superconductors and Josephson junctions with intrinsic spin orbit coupling, Phys. Rev. B **92**, 125443 (2015).

[16] F. S. Bergeret and I. V. Tokatly, Spin-orbit coupling as a source of long-range triplet proximity effect in superconductor-ferromagnet hybrid structures, Phys. Rev. B **89**, 134517 (2014).

[17] M. Alidoust and K. Halterman, Spontaneous edge accumulation of spin currents in finite-size two-dimensional diffusive spin orbit coupled SFS heterostructures, New J. Phys. **17**, 033001 (2015).

[18] P. Hogl, A. Matos-Abiague, I. Zutic, and J. Fabian, Magnetoanisotropic Andreev Reflection in Ferromagnet-Superconductor Junctions, Phys. Rev. Lett. **115**, 116601 (2015).

[19] M. Alidoust and K. Halterman, Long-range spin-triplet correlations and edge spin currents in diffusive spin orbit coupled SNS hybrids with a single spin-active interface, J. Phys.: Condens. Matter **27**, 235301 (2015).

[20] G. C. Paul, P. Dutta, and A. Saha, Transport and noise properties of a normal metal-superconductor-normal metal junction with mixed singlet and chiral triplet pairings, arXiv:1606.06270.

[21] G. Tkachov, Magnetoelectric Andreev effect due to proximity-induced non-unitary triplet superconductivity in helical metals, arXiv:1607.05880.

[22] A. H. Castro Neto, F. Guinea, N. M. R. Peres, K. S. Novoselov, and A. K. Geim, The electronic properties of graphene, Rev. Mod. Phys. **81**, 109 (2009).

[23] C. W. J. Beenakker, Andreev reflection and Klein tunneling in graphene, Rev. Mod. Phys. **80**, 1337 (2008).

[24] B. Z. Rameshti and M. Zareyan, Charge and spin Hall effect in spin chiral ferromagnetic graphene, Appl. Phys. Lett. **103**, 132409 (2013).

[25] N. Tombros, C. Jozsa, M. Popinciuc, H. T. Jonkman, and B. J. van Wees, Electronic spin transport and spin precession in single

graphene layers at room temperature, Nature (London) **448**, 571 (2007).
[26] X.-F. Wang and T. Chakraborty, Collective excitations of Dirac electrons in a graphene layer with spin orbit interactions, Phys. Rev. B **75**, 033408 (2007).
[27] H. B. Heersche, P. Jarillo-Herrero, J. B. Oostinga, L. M. K. Vandersypen, and A. F. Morpurgo, Induced superconductivity in graphene, Solid State Commun. **143**, 72 (2007).
[28] S. Dedkov, M. Fonin, U. Rudiger, and C. Laubschat, Rashba Effect in the Graphene/Ni (111) System, Phys. Rev. Lett. **100**, 107602 (2008).
[29] A. Varykhalov, D. Marchenko, M. R. Scholz, E. D. L. Rienks, T. K. Kim, G. Bihlmayer, J. Sánchez-Barriga, and O. Rader, Ir (111) Surface State With Giant Rashba Splitting Persists Under Graphene in Air, Phys. Rev. Lett. **108**, 066804 (2012).
[30] A. Avsar, J. Y. Tan, T. Taychatanapat, J. Balakrishnan, G. K. W. Koon, Y. Yeo, J. Lahiri, A. Carvalho, A. S. Rodin, E. C. T. OFarrell, G. Eda, A. H. Castro Neto, and B. Ozyilmaz, Spin orbit proximity effect in graphene, Nat. Commun. **5**, 4875 (2014).
[31] Z. Wang, C. Tang, R. Sachs, Y. Barlas, and J. Shi, Proximity-induced Ferromagnetism in Graphene Revealed by the Anomalous Hall Effect, Phys. Rev. Lett. **114**, 016603 (2015).
[32] L. Razzaghi and M. V. Hosseini, Quantum transport of Dirac fermions in graphene with a spatially varying Rashba spin orbit coupling, Physica E **72**, 89 (2015).
[33] J. B. S. Mendes, O. Alves Santos, L. M. Meireles, R. G. Lacerda, L. H. Vilela-Leo, F. L. A. Machado, R. L. Rodrguez-Surez, A. Azevedo, and S. M. Rezende, Spin-Current to Charge-Current Conversion and Magnetoresistance in a Hybrid Structure of Graphene and Yttrium Iron Garnet, Phys. Rev. Lett. **115**, 226601 (2015).
[34] S. Dushenko, H. Ago, K. Kawahara, T. Tsuda, S. Kuwabata, T. Takenobu, T. Shinjo, Y. Ando, and M. Shiraishi, Gate-Tunable Spin-Charge Conversion and the Role of Spin-Orbit Interaction in Graphene, Phys. Rev. Lett. **116**, 166102 (2016).
[35] V. Edelstein, Spin polarization of conduction electrons induced by electric current in two-dimensional asymmetric electron systems, Solid State Commun. **73**, 233 (1990).
[36] N. M. R. Peres, The transport properties of graphene: An introduction, Rev. Mod. Phys. **82**, 2673 (2010).
[37] V. M. Pereira, A. H. Castro Neto, and N. M. R. Peres, Tight-binding approach to uniaxial strain in graphene, Phys. Rev. B **80**, 045401 (2009).
[38] Y. Jiang, T. Low, K. Chang, M. I. Katsnelson, and F. Guinea, Generation of Pure Bulk Valley Current in Graphene, Phys. Rev. Lett. **110**, 046601 (2013).
[39] M. M. Gruji, M. Z. Tadic, and F. M. Peeters, Spin-Valley Filtering in Strained Graphene Structures With Artificially Induced Carrier Mass and Spin-Orbit Coupling, Phys. Rev. Lett. **113**, 046601 (2014).
[40] J. L. Maes, F. de Juan, M. Sturla, and M. A. H. Vozmediano, Generalized effective Hamiltonian for graphene under nonuniform strain, Phys. Rev. B **88**, 155405 (2013).
[41] J. Wang, K. S. Chan, and Z. Lin, Quantum pumping of valley current in strain engineered graphene, Appl. Phys. Lett. **104**, 013105 (2014).
[42] C. Benjamin, How to detect a genuine quantum pump effect in graphene?, Appl. Phys. Lett. **103**, 043120 (2013).
[43] G. J. Verbiest, S. Brinker, and C. Stampfer, Uniformity of the pseudomagnetic field in strained graphene, Phys. Rev. B **92**, 075417 (2015).
[44] M. Assili, S. Haddad, and W. Kang, Electric field-induced valley degeneracy lifting in uniaxial strained graphene: Evidence from magnetophonon resonance, Phys. Rev. B **91**, 115422 (2015).
[45] S. Zhu, J. A. Stroscio, and T. Li, Programmable Extreme Pseudomagnetic Fields in Graphene by a Uniaxial Stretch, Phys. Rev. Lett. **115**, 245501 (2015).
[46] R. Mohammadkhani, B. Abdollahipour, and M. Alidoust, Strain-controlled spin and charge pumping in graphene devices via spin-orbit coupled barriers, Europhys. Lett. **111**, 67005 (2015).
[47] F. Sattari, Spin transport in graphene superlattice under strain, J. Magn. Magn. Mater. **414**, 19 (2016).
[48] C. W. J. Beenakker, Specular Andreev Reflection in Graphene, Phys. Rev. Lett. **97**, 067007 (2006).
[49] K. Halterman, O. Valls, and M. Alidoust, Spin-Controlled Superconductivity and Tunable Triplet Correlations in Graphene Nanostructures, Phys. Rev. Lett. **111**, 046602 (2013).
[50] K. Halterman, O. T. Valls, and M. Alidoust, Characteristic energies, transition temperatures, and switching effects in clean SNS graphene nanostructures, Phys. Rev. B **84**, 064509 (2011).
[51] M. Alidoust and J. Linder, Tunable supercurrent at the charge neutrality point via strained graphene junctions, Phys. Rev. B **84**, 035407 (2011).
[52] M. Zareyan, H. Mohammadpour, and A. G. Moghaddam, Andreev-Klein reflection in graphene ferromagnet-superconductor junctions, Phys. Rev. B **78**, 193406 (2008).
[53] Y. S. Ang, L. K. Ang, C. Zhang, and Z. Ma, Nonlocal transistor based on pure crossed Andreev reflection in a EuO-graphene/superconductor hybrid structure, Phys. Rev. B **93**, 041422(R) (2016).
[54] L. Majidi and R. Asgari, Valley-and spin-switch effects in molybdenum disulfide superconducting spin valve, Phys. Rev. B **90**, 165440 (2014).
[55] K. Halterman, P. H. Barsic, and O. T. Valls, Odd Triplet Pairing in Clean Superconductor/Ferromagnet Heterostructures, Phys. Rev. Lett. **99**, 127002 (2007).
[56] K. Halterman, O. T. Valls, and P. H. Barsic, Induced triplet pairing in clean s-wave superconductor/ferromagnet layered structures, Phys. Rev. B **77**, 174511 (2008).
[57] C. Visani, Z. Sefrioui, J. Tornos, C. Leon, J. Briatico, M. Bibes, A. Barthelemy, J. Santamaria, and Javier E. Villegas, Equal-spin Andreev reflection and long-range coherent transport in high-temperature superconductor-half metallic ferromagnet junctions, Nat. Phys. **8**, 539 (2012).
[58] X. Wu and H. Meng, Gate-voltage control of equal-spin Andreev reflection in half metal-semiconductor-superconductor junctions, Phys. Lett. A **380**, 1672 (2016).
[59] G. E. Blonder, M. Tinkham, and T. M. Klapwijk, Transition from metallic to tunneling regimes in superconducting microconstrictions: Excess current, charge imbalance, and supercurrent conversion, Phys. Rev. B **25**, 4515 (1982).
[60] M. Salehi and G. Rashedi, Spin-polarized conductance in graphene-based FSF junctions, Physica C **470**, 703 (2010).